Decadal Evolution of Ocean Thermal Anomalies in the North Atlantic: The Effects of Ekman, Overturning, and Horizontal Transport

RICHARD G. WILLIAMS AND VASSIL ROUSSENOV

School of Environmental Sciences, University of Liverpool, Liverpool, United Kingdom

DOUG SMITH

Hadley Centre, Exeter, United Kingdom

M. SUSAN LOZIER

Duke University, Durham, North Carolina

(Manuscript received 21 April 2012, in final form 4 September 2013)

ABSTRACT

Basin-scale thermal anomalies in the North Atlantic, extending to depths of 1–2 km, are more pronounced than the background warming over the last 60 years. A dynamical analysis based on reanalyses of historical data from 1965 to 2000 suggests that these thermal anomalies are formed by ocean heat convergences, augmented by the poorly known air–sea fluxes. The heat convergence is separated into contributions from the horizontal circulation and the meridional overturning circulation (MOC), the latter further separated into Ekman and MOC transport minus Ekman transport (MOC-Ekman) cells. The subtropical thermal anomalies are mainly controlled by wind-induced changes in the Ekman heat convergence, while the subpolar thermal anomalies are controlled by the MOC-Ekman heat convergence; the horizontal heat convergence is generally weaker, only becoming significant within the subpolar gyre. These thermal anomalies often have an opposing sign between the subtropical and subpolar gyres, associated with opposing changes in the meridional volume transport driving the Ekman and MOC-Ekman heat convergences. These changes in gyre-scale convergences in heat transport are probably induced by the winds, as they correlate with the zonal wind stress at gyre boundaries.

1. Introduction

Over the last few decades, there has been a significant warming of the ocean over the globe, which is particularly pronounced over the North Atlantic (Levitus et al. 2012). Regional variability in heat storage, however, is more pronounced than the global signal and involves either an opposing pattern of warming and cooling between the subpolar and subtropical gyres or the same signed response over the entire basin (Fig. 1). These thermal anomalies persist from several years to decades and extend over the thermocline (the upper 1–2 km of the ocean); deeper anomalies might have also occurred, but they are not detectable in the sparser observations at depth.

In this study, we explore whether the decadal changes in ocean heat storage in the North Atlantic are controlled by changes in ocean heat convergence, rather than by air–sea heat fluxes. The heat convergence is achieved via a combination of vertical and horizontal cells (Bryden and Imawaki 2001): the vertical cell, referred to as the meridional overturning circulation (MOC), involves a northward transfer of warmer upper waters and a southward return of cooler deeper waters, while the horizontal cell involves a northward transfer of warmer waters and southward return of cooler waters at the same depth. To gain insight into how the thermal anomalies are formed, we identify the explicit wind-driven contribution, separating the heat transfer by the vertical cell into Ekman and MOC transport minus Ekman transport (MOC-Ekman) components. This separation makes more explicit the subtropical overturning

Denotes Open Access content.

Corresponding author address: Richard G. Williams, Department of Earth, Ocean and Ecological Sciences, School of Environmental Sciences, University of Liverpool, Liverpool, L69 3GP, United Kingdom.
E-mail: ric@liv.ac.uk

DOI: 10.1175/JCLI-D-12-00234.1

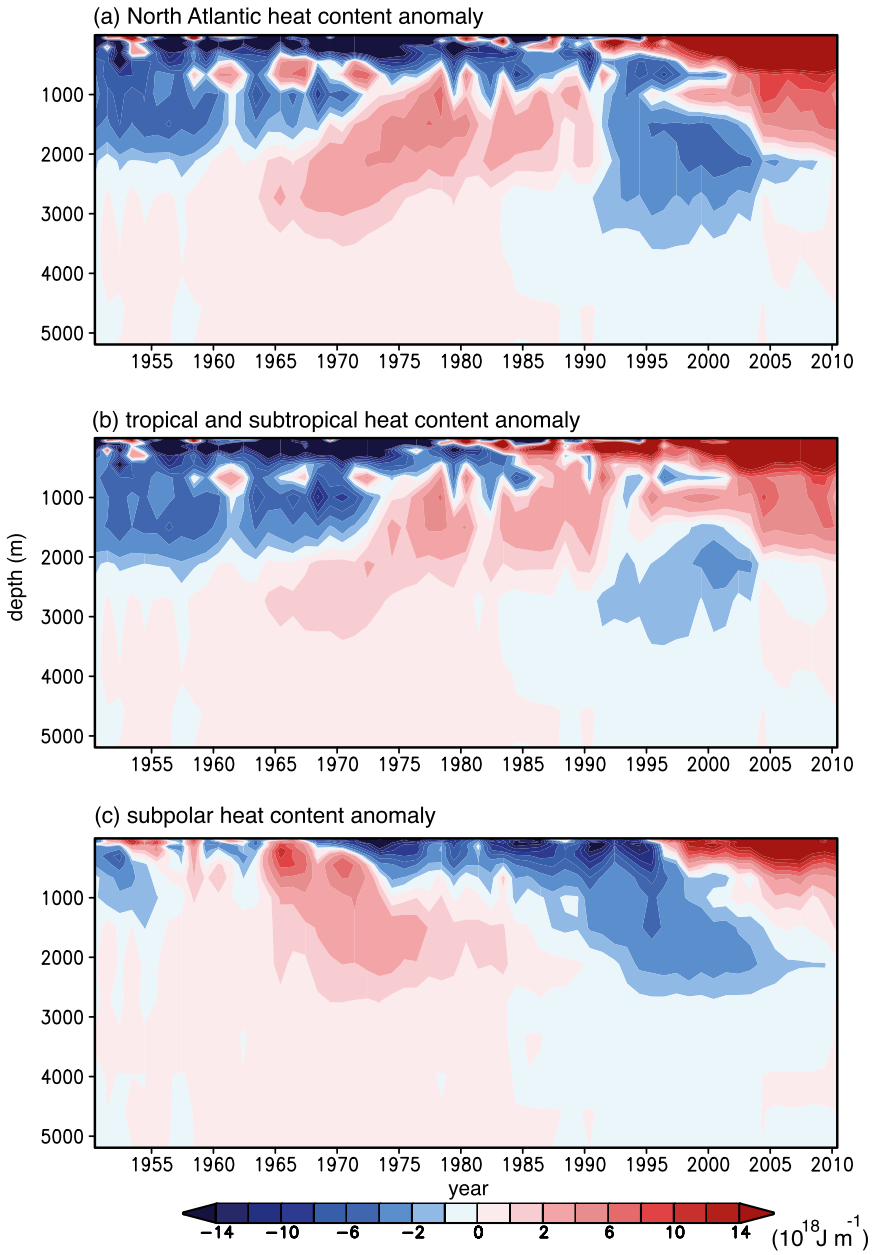

FIG. 1. Time series of North Atlantic Ocean heat content anomaly integrated zonally across the basin and 1.25° of latitude (10^{18} J m^{-1}; red is warmer and blue is cooler) vs depth (m) from 1950 to 2010 for (a) the entire domain (0°–89°N), (b) the tropics and subtropics (0°–45°N), and (c) the subpolar region (46°–89°N) derived from the Met Office hydrographic dataset (appendix). The anomaly is defined for each depth relative to a time mean from 1950 to 2010. Note that the thermal response of the tropics and subtropics in (b) dominates the response of the entire basin in (a) because of the greater volume weighting.

cell, as discussed by Talley (1999), Klinger and Marotzke (2000), and Czaja and Marshall (2006).

The paper is set out as follows: thermal anomalies over the subtropical and subpolar latitudes are diagnosed from historical data in the North Atlantic (section 2); the link between the evolution of thermal anomalies and the meridional convergence of heat transport is assessed by dynamically assimilating analyses of temperature and salinity data into a circulation model from 1965 to 2010 (section 3); the heat transport is partitioned into horizontal and vertical cells with the latter further separated into an Ekman cell and an MOC-Ekman cell (section 4);

the temporal and spatial character of the different heat transport components are identified, as well as the effect of heat convergence anomalies in the subtropical and subpolar gyres (section 5); and finally, the wider implications of the study are discussed (section 6).

2. Historical heat content changes

Historical temperature and salinity changes in the North Atlantic Ocean are examined using a global analysis of the available hydrographic data (Boyer et al. 2006) and recent Argo data from the Met Office from 1950 to 2010 (Ingleby and Huddleston 2007; Smith and Murphy 2007). The analysis fills in data-sparse regions by extrapolating from the observational data using a covariance field from the Hadley Centre model, where the covariance is based on repeated model ensemble integrations with perturbed physical parameters to gain additional skill (Smith and Murphy 2007; Smith et al. 2010); for further details and sensitivity to Argo, see the appendix. These temperature reconstructions are broadly similar to, though smoother than, those constructed from the HydroBase dataset based solely on hydrographic data, reported for two periods, 1950–70 and 1980–2000, by Lozier et al. (2008).

Over the North Atlantic, basin-integrated thermal anomalies over the upper 3.5 km reverse in sign over the temporal record (Fig. 1a): cool anomalies occur from 1950 to the early 1960s and during the mid-1990s, separated by warm anomalies from the mid-1970s to 1990, followed by a warm anomaly from 1995 to 2010. These anomalies extend from the surface to depths of 1–2 km within the thermocline and are not a simple reflection of the sea surface temperature signal, suggesting that advection is playing a key role in determining their distribution.

While there are these decadal changes with opposing signs over the entire North Atlantic, there are also often opposing changes between the subtropical and subpolar gyres (Figs. 1b,c): there is a cool anomaly in the subtropical gyre and a slightly warm anomaly in the subpolar gyre from 1955 to 1970, which switches to a warm anomaly in the subtropical gyre and a cool anomaly in the subpolar gyre from 1985 to 1995. There are also periods where a single-signed anomaly extends over the entire basin, such as a warm anomaly spreading over the entire basin from 1995 to 2010. Our aim is to assess how these thermal anomalies might be formed and address why there might be an opposing response in the subtropical and subpolar gyres.

3. Heat balance in the subtropical and subpolar North Atlantic

The mechanisms by which the thermal anomalies evolve, defined in terms of a depth and zonal integral and depicted in Fig. 2a, are now assessed in terms of their heat budget. Ignoring diffusive transfers and the benthic heat flux, there is a three-way balance among the tendency in the depth- and zonally integrated ocean heat content, the meridional convergence in ocean heat transport, and the air–sea heat flux:

$$\int_{-D}^{0} \frac{\partial \overline{\theta}^{x}}{\partial t} dz + \int_{-D}^{0} \frac{\partial}{\partial y} \overline{v\theta}^{x} dz = \frac{\overline{\mathcal{H}}^{x}}{\rho_0 C_p}, \qquad (1)$$

where θ is the potential temperature; D is the depth of the ocean; v is the meridional velocity; $\mathcal{H}$ is the surface heat flux; and ρ_0 and C_p are the reference density and heat capacity, respectively, where the overbar with a superscript x represents a zonal integral. Subsequently, we refer to the depth- and zonally integrated heat content $Q \equiv \rho_0 C_p \int_{-D}^{0} \overline{\theta}^{x} dz$ and the meridional divergence in heat transport $\nabla \cdot (VQ) \equiv \rho_0 C_p \int_{-D}^{0} (\partial/\partial y) \overline{v\theta}^{x} dz$.

To identify the relative importance of ocean heat transport for the evolution of thermal anomalies, we perform a dynamical assimilation of the gridded historical temperature and salinity data from the Met Office, similar in approach to previous diagnostic studies for the North Atlantic (Mellor et al. 1982; Greatbatch et al. 1991). A global version of the Massachusetts Institute of Technology general circulation model (MITgcm; Marshall et al. 1997) is employed with a horizontal resolution of 1° with 23 levels in the vertical, spaced from 10 m apart at the surface to 500 m at depth. For each separate year, the circulation model is initialized with the global analysis of temperature and salinity data from the Met Office, and then integrated forward with monthly wind forcing from the National Centers for Environmental Prediction (NCEP) allowing a dynamically adjusted velocity, temperature, and salinity to form. There is only a slight offset between the zonally and depth-integrated heat content from this assimilation process and that from the original temperature analyses (Fig. 2a, dashed and solid lines). The changes in heat transport are evaluated from the product of the dynamically adjusted velocities and temperatures over an annual cycle and the changes in ocean heat content from changes in the dynamically adjusted temperatures. This model assimilation includes an initial 1-month spinup and then a further 12-month integration to cover an annual cycle, so that diagnostics are applied for months 2–13 (discussed further in the appendix).

The dynamical adjustment does not include explicit surface heat or freshwater fluxes, but does include a weak relaxation to the initial density on a time scale of 36 months throughout the water column. This relaxation minimizes the model drift away from the initial state, but is sufficiently weak to avoid generating spurious

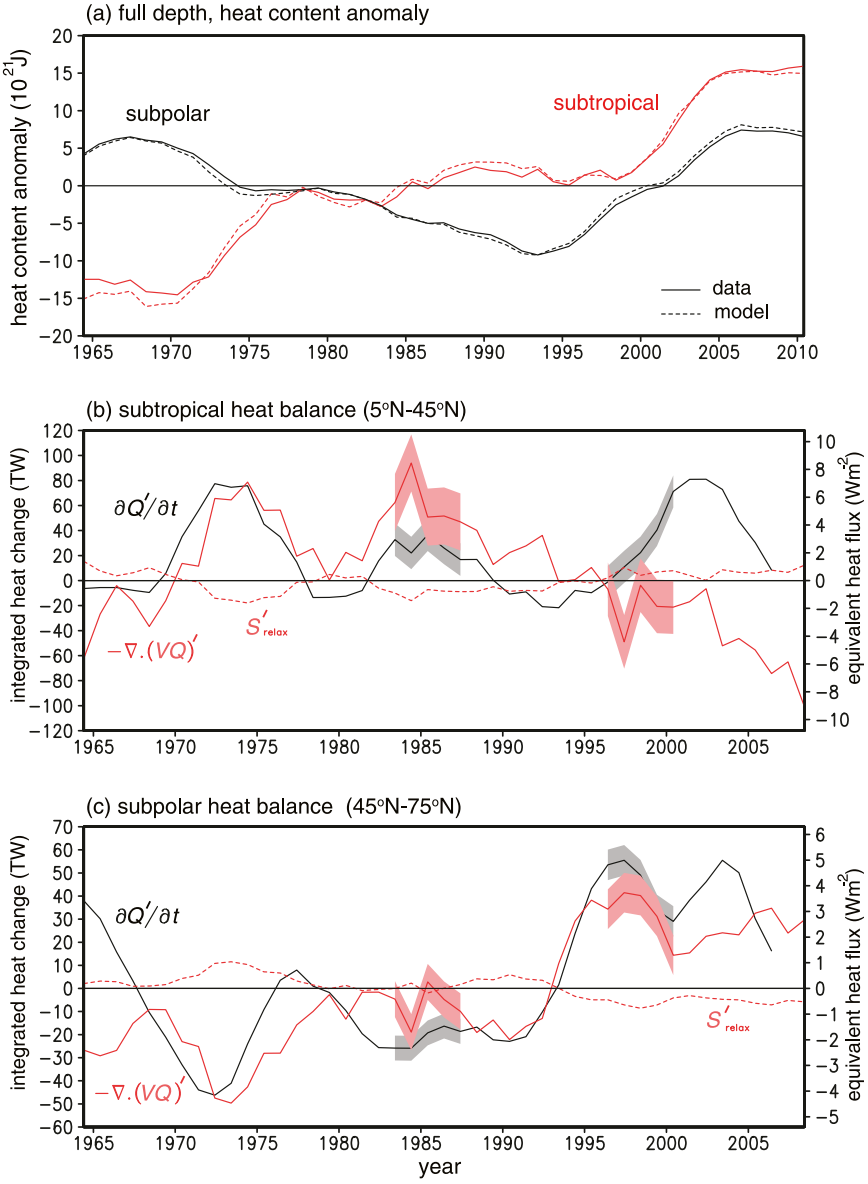

FIG. 2. Time series for (a) full depth- and zonally integrated heat content anomaly $Q'(t)$ (10^{21} J) for the tropics and subtropics (5°–45°N; red line) and subpolar region (45°–75°N; black line) from 1965 to 2010 based on temperature analyses (solid line) and after a model assimilation (dashed line); and volume-integrated heat content tendency $\partial Q'/\partial t$ (TW; where 1 TW = 10^{12} W; black line), convergence in heat transport $-\nabla \cdot (VQ)'$ (red line), and change due to thermal relaxation S'_{relax} (red dashed line) for (b) the tropics and subtropics (5°–45°N) and (c) the subpolar region (45°–75°N). In (b),(c), the left-hand y axis is the volume-integrated heat uptake (TW) and the right-hand y axis is the equivalent heat flux per unit horizontal area ($W\,m^{-2}$). Diagnostics are based on 5-yr running means. The tendency is evaluated from the difference between the average of Q' over 5-yr bins and so extends over a shorter time period. The sensitivity to perturbations in the temperature data (based on a 95% confidence interval from 2 standard errors in the historical data) is included by the gray and red shading for two 5-yr periods at 1985 and 1998.

depth-integrated circulation from bottom flows interacting with topography.

Our model assimilations include two approximations that merit further discussion. The model assimilation experiments are performed at a non-eddy-permitting resolution of 1°, so that the representation of the Gulf Stream is relatively coarse and leads to horizontal errors in the distribution of the thermal anomaly. Our focus

TABLE 1. Correlations of $\partial Q'/\partial t$ with $-\nabla \cdot (VQ)'$ and the temporal anomalies in air–sea heat fluxes from NCEP and ECMWF, evaluated over the tropics and subtropics (5°–45°N) and the subpolar region (45°–75°N). All fields are detrended and 5-yr running means are applied for the period from 1965 to 2010. Correlations are shown in italic if less than ±0.34 (98% confidence limit) and in boldface if greater than ±0.37 (99% confidence limit); confidence limits are based upon each annual realization being viewed as independent. The European Centre for Medium-Range Weather Forecasts (ECMWF) fluxes are based upon the 40-yr ECMWF Re-Analysis (ERA-40; 1958–2001) and the Interim ECMWF Re-Analysis (ERA-Interim; 2002–10).

	Subtropical $\partial Q'/\partial t$	Subpolar $\partial Q'/\partial t$
$-\nabla \cdot (VQ)'$	0.35	**0.59**
$\mathcal{H}'_{\mathrm{NCEP}}$	*−0.05*	*0.06*
$\mathcal{H}'_{\mathrm{ECMWF}}$	*0.27*	*0.33*
$-\nabla \cdot (VQ)' + \mathcal{H}'_{\mathrm{NCEP}}$	*−0.05*	*0.32*
$-\nabla \cdot (VQ)' + \mathcal{H}'_{\mathrm{ECMWF}}$	0.37	**0.48**

though is on the zonally and depth-integrated thermal anomaly across each of the gyres, which is probably less sensitive than the local anomalies to model resolution. The second approximation is that our model assimilation experiments are performed annually with the input data from annual averages of monthly reanalyses from the Met Office. Because our focus is on explaining the decadal evolution of the thermal anomalies, we believe that this annual resolution is sufficient.

a. Comparison of heat content tendency and convergence of heat transport

Returning to the zonally and depth-integrated heat balance (1), the tendency of the thermal anomalies and convergence of the meridional heat transport anomalies are separately evaluated over the subpolar latitudes (45°–75°N) and the tropical and subtropical latitudes (5°–45°N). The volume-integrated anomalies in the heat content tendency and convergence in heat transport typically range from ±100 TW over the subtropical to ±50 TW over the subpolar latitudes (Figs. 2b,c), which equates to equivalent surface heat fluxes per unit horizontal area of ±10 and ±5 $\mathrm{W\,m^{-2}}$, respectively. In comparison, the model assimilation includes a relatively weak relaxation to the initial density, providing equivalent heat flux anomalies with a variability of 0.7 $\mathrm{W\,m^{-2}}$ (Figs. 2b,c; dashed line), acting slightly to dampen the effect of the convergence in heat transport.

Over much of the record, there is reasonable agreement between the heat content tendency and heat transport convergence, particularly over the subtropics from 1965 to 1997 (Fig. 2b) and the subpolar latitudes from 1968 to 2005 (Fig. 2c). This agreement is supported by a positive correlation between the tendency in heat content and the convergence in heat transport, reaching 0.35 over the subtropics and 0.59 over the subpolar latitudes, significant at 98% and 99% confidence limits, respectively (Table 1). However, there are periods where there is a mismatch between these terms, after 2000 in the subtropics and close to 1965 in the subpolar latitudes (Figs. 2b,c), implying that air–sea fluxes become important or there are errors in closing the heat budget (1).

The sensitivity in our analyses to the data inputs is assessed by repeating our dynamical assimilations with perturbed temperature data. The perturbations are based on the standard errors from the historical data, which are applied to 5-yr periods centered on 1985 or 1998 for the subtropic and subpolar domains (appendix). These perturbation experiments reveal sensitivities for the heat content tendency and heat convergence typically reaching at least ±10 TW (Table 2; Figs. 2b,c; shading), which are significant when the heat convergences are small, such as close to 2000. There are also additional systematic errors in our methodology and model circulation that are not captured by this sensitivity analysis.

b. Comparison of heat content tendency and air–sea heat fluxes

Reanalysis estimates of the net surface heat flux from ECMWF and NCEP vary by typically ±15 $\mathrm{W\,m^{-2}}$ over the subtropical gyre and ±7 $\mathrm{W\,m^{-2}}$ over the subpolar gyre (Figs. 3a,b). This air–sea contribution is often much larger than the mismatch between the sum of the heat content tendency, the heat transport divergence, and interior density relaxation (Fig. 3, black and dashed lines). The correlation between the heat content tendency and air–sea fluxes is always weaker than that between the heat content tendency and heat convergence (Table 1), only becoming significant over the subpolar gyre for the air–sea fluxes from ECMWF. The correlation

TABLE 2. The $\partial Q'/\partial t$, $-\nabla \cdot (VQ)'$, and $\partial Q'/\partial t + \nabla(VQ)'$ (TW) integrated over the subtropics or subpolar gyres estimated from 36 ensemble model integrations with temperature perturbations for 1985 and 1998: ensemble mean plus/minus the std dev.

	Subtropical		Subpolar	
	1985	1998	1985	1998
$\partial Q'/\partial t$	31.8 ± 6.5	18.2 ± 6.4	−21.2 ± 2.7	55.2 ± 3.3
$-\nabla \cdot (VQ)'$	63.9 ± 11.4	−2.6 ± 10.7	13.9 ± 3.9	60.7 ± 4.3
$\partial Q'/\partial t + \nabla(VQ)'$	−32.1 ± 17.9	20.8 ± 17.1	−35.1 ± 6.6	−5.5 ± 7.6

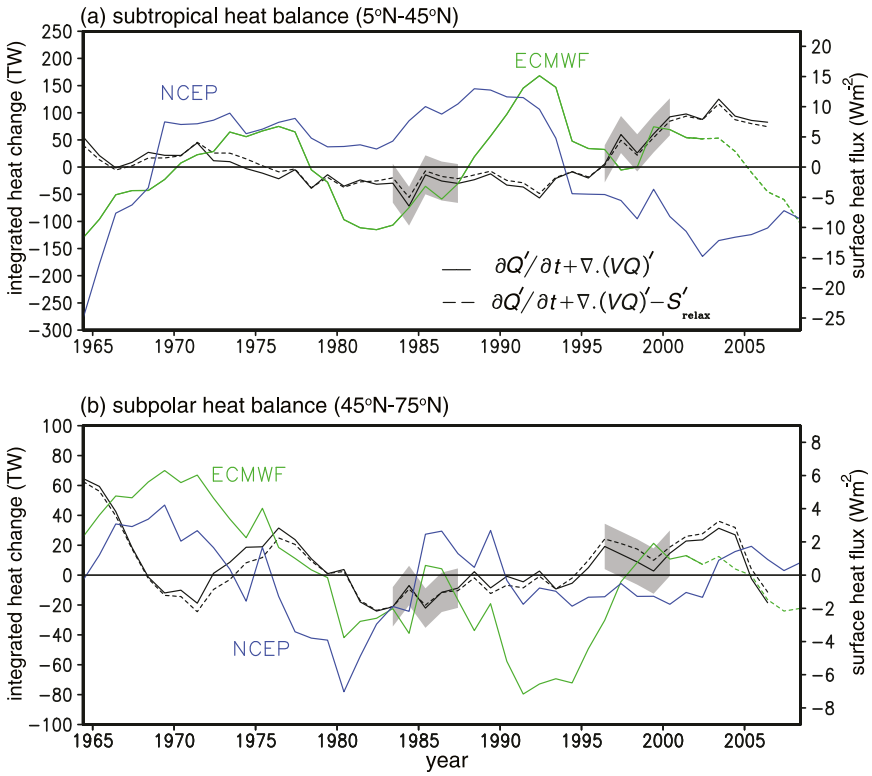

FIG. 3. Time series of North Atlantic Ocean heat balance comparing the sum of the depth- and zonally integrated heat content tendency and divergence in heat transport $\partial Q'/\partial t + \mathbf{\nabla} \cdot (VQ)'$ (black line), and minus the thermal relaxation (black dashed line), and air–sea fluxes from ECMWF (ERA-40 and ERA-Interim, green solid and dashed lines, respectively) and NCEP (blue line) for (a) tropics and subtropics (5°–45°N) and (b) subpolar (45°–75°N) from 1965 to 2010. The left-hand y axis is the area-integrated heat uptake (TW) and the right-hand y axis is the implied surface heat flux per unit horizontal area ($\mathrm{W\,m^{-2}}$). The sensitivity to perturbations in the temperature data is included by the gray shading as in Fig. 2.

between the heat content tendency and the sum of the heat convergence and air–sea fluxes from ECMWF is significant for both the subtropical and subpolar gyres (Table 1), at confidence levels of greater than 98% and 99%, respectively.

Air–sea fluxes are probably much more important in forming thermal anomalies on shorter time scales, such as in how seasonal changes in ocean heat content outside the tropics are explained by air–sea fluxes (Gill and Niller 1973) and in how interannual changes in North Atlantic heat storage are explained by a combination of advection and air–sea fluxes (Piecuch and Ponte 2012).

On decadal time scales, the air–sea fluxes are unable to explain the thermal anomalies for a variety of reasons: 1) air–sea fluxes contain significant errors in their components, for example, errors in latent heat flux alone over the Labrador Sea from ECMWF and NCEP reach 10% and 27% (Renfrew et al. 2010); 2) there is often a significant mismatch between the ECMWF and NCEP reanalyses (Fig. 3, green and blue lines); and 3) the air–sea flux signals are larger than the uncertainties arising from our model experiments with perturbed temperatures (Fig. 3, gray shading). Thus, although we cannot exclude the influence of air–sea fluxes on the formation of thermal anomalies, we subsequently focus on the role of ocean heat transport.

4. Mechanisms of heat transport

Given our view that the tendency in the thermal anomalies is broadly due to the convergence in ocean heat transport (Figs. 2b,c), we now consider the mechanisms by which these changes are achieved.

a. Separating the heat transport into different components

The meridional heat transport is accomplished via a vertical cell, referred to as the meridional overturning circulation, and a horizontal cell involving the horizontal departures in the flow,

$$\rho_0 C_p \int_{-D}^{0} \overline{v\theta}^x \, dz = \rho_0 C_p \underbrace{\int_{-D}^{0} \overline{v}^x \overline{\theta}^x \, dz}_{\text{MOC}} + \rho_0 C_p \underbrace{\int_{-D}^{0} \overline{v'\theta'}^x \, dz}_{\text{horizontal}}, \quad (2)$$

where the product $\rho_0 C_p$ is taken as a constant of $4.09 \times 10^6 \, \text{J K}^{-1} \, \text{m}^{-3}$ from a basin average; the prime represents a horizontal deviation from the zonal integral across the basin; and the zonal integrals for $\overline{v}^x$, $\overline{\theta}^x$, and the horizontal heat flux $\overline{v'\theta'}^x$ all vary with depth.

The MOC results from both Ekman and geostrophic flows (see Fig. 5a, described in greater detail below). Here, we choose to separate the direct effect of the winds on the MOC contribution by defining the Ekman meridional heat transport as

$$\rho_0 C_p \int_{-h_{\text{ek}}}^{0} \overline{v}^x_{\text{ek}} \overline{\theta}^x \, dz + \rho_0 C_p \int_{-D}^{-h_{\text{ek}}} \overline{v}^x_r \overline{\theta}^x \, dz, \quad (3)$$

involving the heat transfer from the Ekman flow v_{ek} in the surface Ekman layer of thickness h_{ek}, and the deeper return flow v_r, varying with depth and extending to the sea floor D. The volume flux V_{ek} carried in the surface Ekman layer is equal and opposite to the return volume flux below the Ekman layer, $V_{\text{ek}} \equiv \int_{-h_{\text{ek}}}^{0} v_{\text{ek}} \, dz = -\int_{-D}^{-h_{\text{ek}}} v_r \, dz$, so that the Ekman meridional heat transport can be written more concisely as

$$\rho_0 C_p \overline{V}^x_{\text{ek}} (\overline{\theta}^x_{\text{ek}} - \overline{\theta}^{x,z}_r), \quad (4)$$

where θ_{ek} and θ_r are the potential temperatures of the Ekman layer and return flow, and $\overline{\theta}^{x,z}_r$ includes averaging the temperature of the return flow both zonally and with depth below the Ekman layer, such that $\overline{\theta}^{x,z}_r \equiv \int_{-D}^{-h_{\text{ek}}} \overline{v}^x_r \overline{\theta}^x \, dz / \int_{-D}^{-h_{\text{ek}}} \overline{v}^x_r \, dz$.

The total meridional heat transport can then be rewritten in terms of three contributions, combining (2) with the definition of the Ekman meridional heat transport (4), as

$$\rho_0 C_p \int_{-D}^{0} \overline{v\theta}^x \, dz = \rho_0 C_p \left\{ \underbrace{\left[\int_{-D}^{0} \overline{v}^x \overline{\theta}^x \, dz - \overline{V}^x_{\text{ek}} (\overline{\theta}^x_{\text{ek}} - \overline{\theta}^{x,z}_r) \right]}_{\text{MOC-Ekman}} + \underbrace{\overline{V}^x_{\text{ek}} (\overline{\theta}^x_{\text{ek}} - \overline{\theta}^{x,z}_r)}_{\text{Ekman}} + \underbrace{\int_{-D}^{0} \overline{v'\theta'}^x \, dz}_{\text{horizontal}} \right\}. \quad (5)$$

This decomposition of the meridional heat transport is attractive as each of the components is expected to vary in a different manner. The Ekman cell measures the direct effect of the winds, particularly varying over the gyre scale. Instead, the MOC-Ekman cell is associated with west–east contrasts in density across the basin (Marotzke et al. 1999), affected by basin-scale contrast in buoyancy forcing and indirectly by wind-driven changes in the circulation.

b. Different choices for the Ekman return cell

The separation of the heat transport (5) into MOC-Ekman, Ekman, and horizontal components is handicapped by the ambiguity in determining the depth structure of the Ekman cell, expressed in terms of the temperature of the return flow θ_r in (4). If this term is ignored by setting $\theta_r = 0$, then the Ekman heat flux through the section has an associated mass flux and its value is sensitive to the choice of the temperature units. Instead, we choose to separate the heat transport components and solve for the Ekman cell using a mass-conserving framework.

The appropriate choice for the Ekman return cell and associated temperature depends on the time scale of interest. Idealized wind-driven experiments suggest that a sudden increase in winds induces a rapid spinup of the entire water column, involving barotropic Rossby waves propagating westward across the basin on the time scale of several days, followed by slower, baroclinic Rossby waves crossing the basin on the time scale of several years (Anderson and Gill 1975).

Thus, there are two plausible limits to consider for the Ekman return flow. First, on time scales of a few days or weeks, the Ekman flow can be assumed to be returned uniformly with depth given the spinup of the entire water column (Jayne and Marotzke 2001); this limit is applied in interpreting the observational records from the Rapid Climate Change (RAPID) array of moored instruments deployed along 26.5°N (Cunningham et al. 2007; Kanzow et al. 2007). Second, on time scales of several decades, the Ekman flow over the subtropical gyre can be assumed to be returned within the upper thermocline along subducted isopycnals; this idealized thermocline view has been applied in diagnosing the subtropical overturning cell from observations (Talley

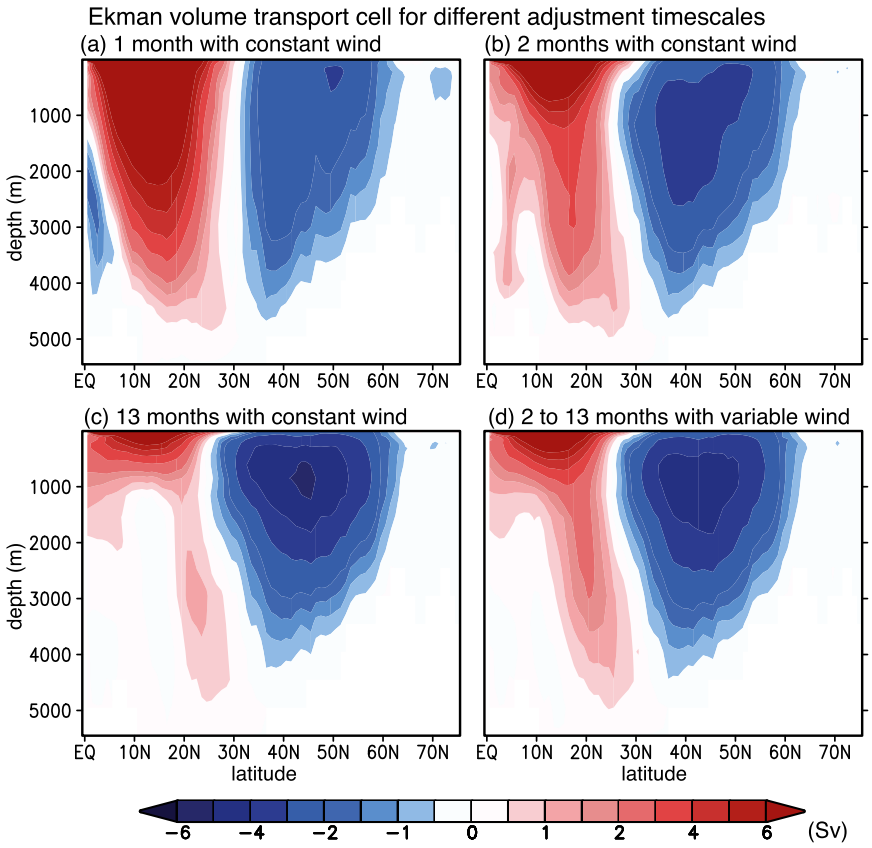

FIG. 4. Diagnostics of the Ekman volume transport cell (Sv) from the zonally integrated difference in velocity in a twin experiment with and without winds: (a)–(c) after 1, 2, and 13 months, respectively, for constant climatological winds, and (d) for 2–13 months for monthly varying climatological winds.

1999) and in providing a closure for its strength (Klinger and Marotzke 2000).

For our study, we are interested on time scales from several years to decades, so we choose to solve for the Ekman cell, rather than assume its depth structure. The Ekman circulation and its return flow are diagnosed in twin general circulation experiments involving an assimilation of the density data, either including or excluding wind forcing. In the experiment with wind forcing, the dynamical adjustment includes the surface Ekman response and a deeper return flow, whereas the accompanying experiment without winds automatically omits the Ekman cell.

An Ekman streamfunction is diagnosed from the difference in the zonal integral of the velocities between the wind and no wind experiments, revealing two overturning cells centered on the boundary of the subtropical gyre: surface flow directed northward at 15°N and southward at 45°N (Fig. 4). The southern Ekman cell becomes more surface intensified with time (Figs. 4a–c). In broad agreement, Klinger and Marotzke (2000), using a similar approach with model experiments integrated to a steady state, obtain similar Ekman cells that are more surface intensified, extending to depths of 200 m and the upper 1 km on the southern and northern flanks of the subtropical gyre respectively.

In our subsequent diagnostics for the heat transport and its components, the model experiments include an initial spinup of 1 month plus an annual cycle, so that the Ekman cell is estimated from an annual average of the zonal integral of the velocity differences from months 2 to 13 (Fig. 4d), because our interest ranges from interannual to decadal changes in heat transport.

5. Partitioning of heat transport

The heat transport is next partitioned into its separate components for a climate mean extending from 1965 to 2010, and then the effect of these components in forming the subtropical and subpolar thermal anomalies is assessed.

a. Climate mean

The MOC, defined by the meridional volume transport above 1300 m, is directed northward throughout the basin and reaches 17.5 Sv (1 Sv $\equiv 10^6\,\mathrm{m^3\,s^{-1}}$) between

40° and 50°N (Fig. 5a). The MOC includes a surface Ekman transport, from the zonal integral of $-\tau_x/(\rho f)$, and a geostrophic transport, where the surface Ekman transport is northward reaching 15 Sv at 15°N and southward reaching −3 Sv from 35° to 55°N; here, τ_x is the eastward wind stress and f is the Coriolis parameter.

The total heat transport (3) from the MOC and horizontal transfer reaches 0.8 PW at 15°N and decreases to 0.7 PW at 40°N (Fig. 5b, black line). This estimate is relatively weak compared with observational estimates of 1.3 ± 0.3 PW at 26°N from section data (Hall and Bryden 1982). Our underestimate of heat transport probably reflects the model horizontal resolution of 1°, which underestimates the strength of the Gulf Stream and its accompanying heat transport, rather than any missing mesoscale eddy transfer of heat; this view is supported by eddy-resolving model experiments at 1/12° that yield a poleward ocean heat transport of 1.2 PW, of which the eddies only directly transfer −0.1 PW (Rhein et al. 2011).

The heat transport by the MOC provides the dominant contribution over most of the North Atlantic (Fig. 5b, blue line), while the heat transport by the horizontal cell only becomes important over the subpolar latitudes, reaching 0.35 PW at 55°N (Fig. 5b, red line).

The heat transport by the overturning cell (5) is further separated into contributions from the Ekman cell and the MOC-Ekman cell: the Ekman heat transport (4) provides a large northward heat transport of 0.7 PW at 13°N and −0.3 PW at 37°N (Fig. 5c, green line), while the heat transport by the MOC-Ekman cell has a local maximum within the subtropical gyre reaching 0.95 PW at 37°N (Fig. 5c, blue line).

Hence, the meridional heat transport for the climate mean is achieved via three different components: the Ekman cell dominates in the tropics, the MOC-Ekman in the midlatitudes, and the horizontal cell in the high latitudes.

The relative importance of each heat transport component alters slightly when considering the temporal variability of these components. The standard deviation of the heat transport reaches 9% of the climate mean, 70 TW in the tropics (Fig. 5d, black line), and is mainly due to variations in the Ekman component. Piecuch and Ponte (2012) obtain broadly similar interannual variations in heat transport (10%–20% of their climate mean).

b. Spatial pattern of the heat transport variability

The thermal anomalies change in sign over the North Atlantic between the subtropical and subpolar gyres from 1965 to 2010 (Figs. 1 and 6a). There is a cold anomaly over the subtropics and warm anomaly over the subpolar gyre up to 1975, then a weaker warm anomaly in the subtropics and a cold anomaly in the subpolar up to 2000. In turn, there is a broadly similar pattern in the northward Ekman heat transfer: a negative anomaly over the subtropics and positive anomaly over the subpolar gyre up to 1970, then a generally positive anomaly over the subtropics and more negative anomaly over the subpolar gyre (Fig. 6b).

In contrast, the MOC-Ekman heat transfer often has the opposing sign to that of the Ekman heat transfer, and is generally enhanced in the subtropics up to 1970 and then weakened up to 1995 (Fig. 6c). There are also periods when the MOC-Ekman heat transport anomaly extends over much of the basin, such as the negative anomaly from 1973 to 1980 and the positive anomalies from 1995 to 2000 and 2005 to 2010.

The horizontal heat transfer is much weaker than the Ekman and MOC-Ekman heat components over most of the basin, but provides a more significant contribution north of 60°N (Fig. 6d). The horizontal heat transfer changes sign frequently across the basin, particularly vanishing across 45°N (the subtropical–subpolar boundary), as well as within the gyre.

In summary, each of the heat transport components has a different character: the Ekman heat transport peaks at low latitudes and its anomaly changes sign across the subtropical–subpolar boundary; the MOC-Ekman heat transport peaks at the midlatitudes and its anomaly either has a basinwide or a gyre response, the latter often in the opposite sense to the Ekman response; and the horizontal heat transport peaks at high latitudes and has an opposing pattern within and between the gyres.

The relationship between the Ekman and MOC-Ekman transfer is next addressed, followed by their effect on the gyre-integrated thermal anomalies revisited and then their connection to the large-scale winds.

c. Variations in the Ekman and MOC-Ekman volume and heat transfer

Our analysis of the heat transports over the basin reveals the larger contributions of the Ekman and MOC-Ekman heat transfer, compared with the smaller contribution from horizontal transfer. While the Ekman and MOC-Ekman contributions are noisy, they often have a different response over each gyre.

To gain some insight into these gyre-scale variations, consider how the meridional volume transport varies for different depth ranges. Over the upper 100 m, there are interannual and decadal variations in the volume transport (Fig. 7a), which are much larger in magnitude at 5° than at 45°N, broadly following that expected from the wind-driven Ekman response (Fig. 7a, dashed line).

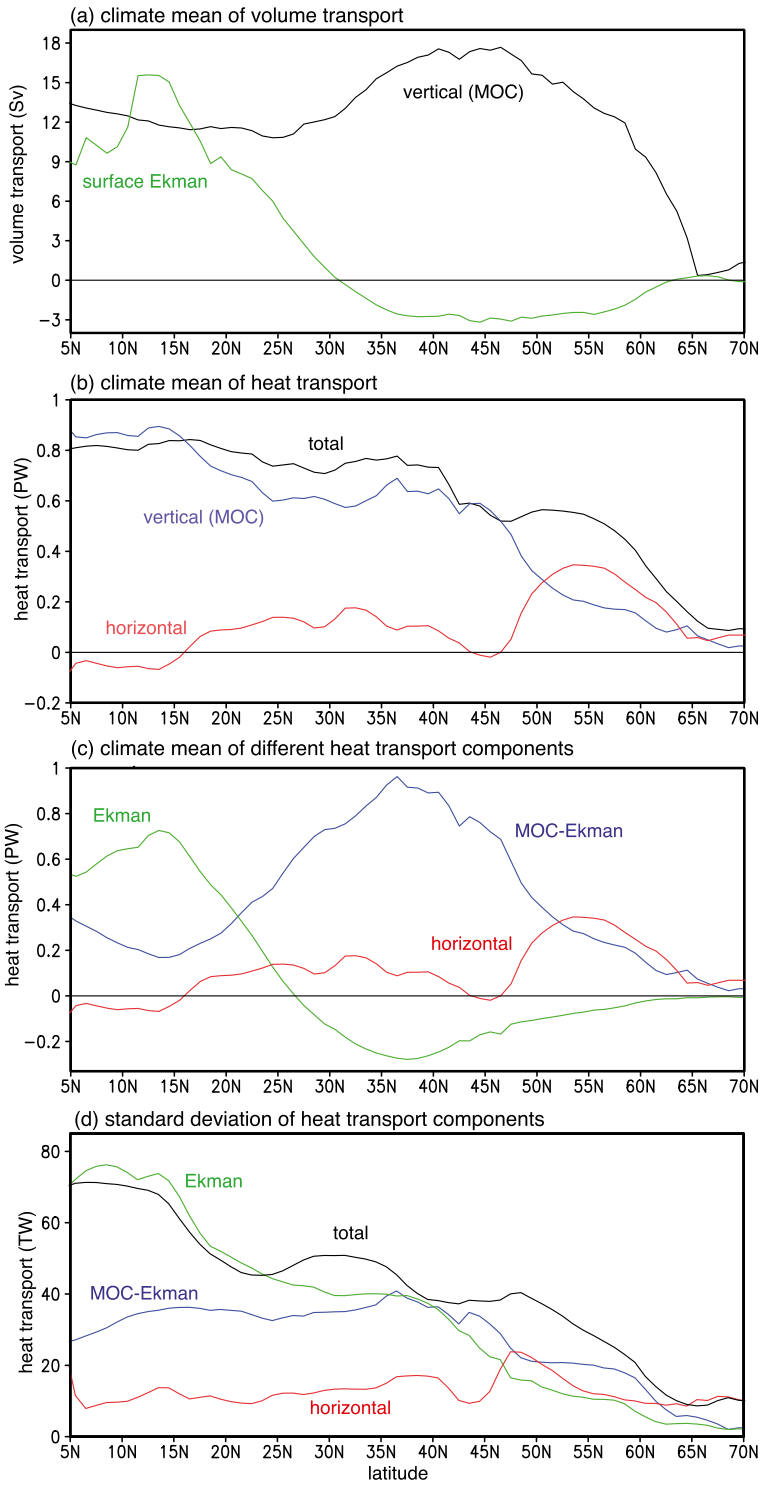

FIG. 5. Climate-mean diagnostics for 1965–2010 based on a dynamical assimilation of densities repeated for each year: (a) volume transport (Sv) separated into the vertical cell (MOC; black) integrated over the upper 1300 m and the surface Ekman transport over the upper 20 m (green); depth-integrated heat transport (PW; black) separated into either (b) vertical (MOC; blue) and horizontal (red) components or (c) Ekman (green), MOC-Ekman (blue), and horizontal (red) components, and (d) std dev of the heat transport (black) and its components for each year (TW).

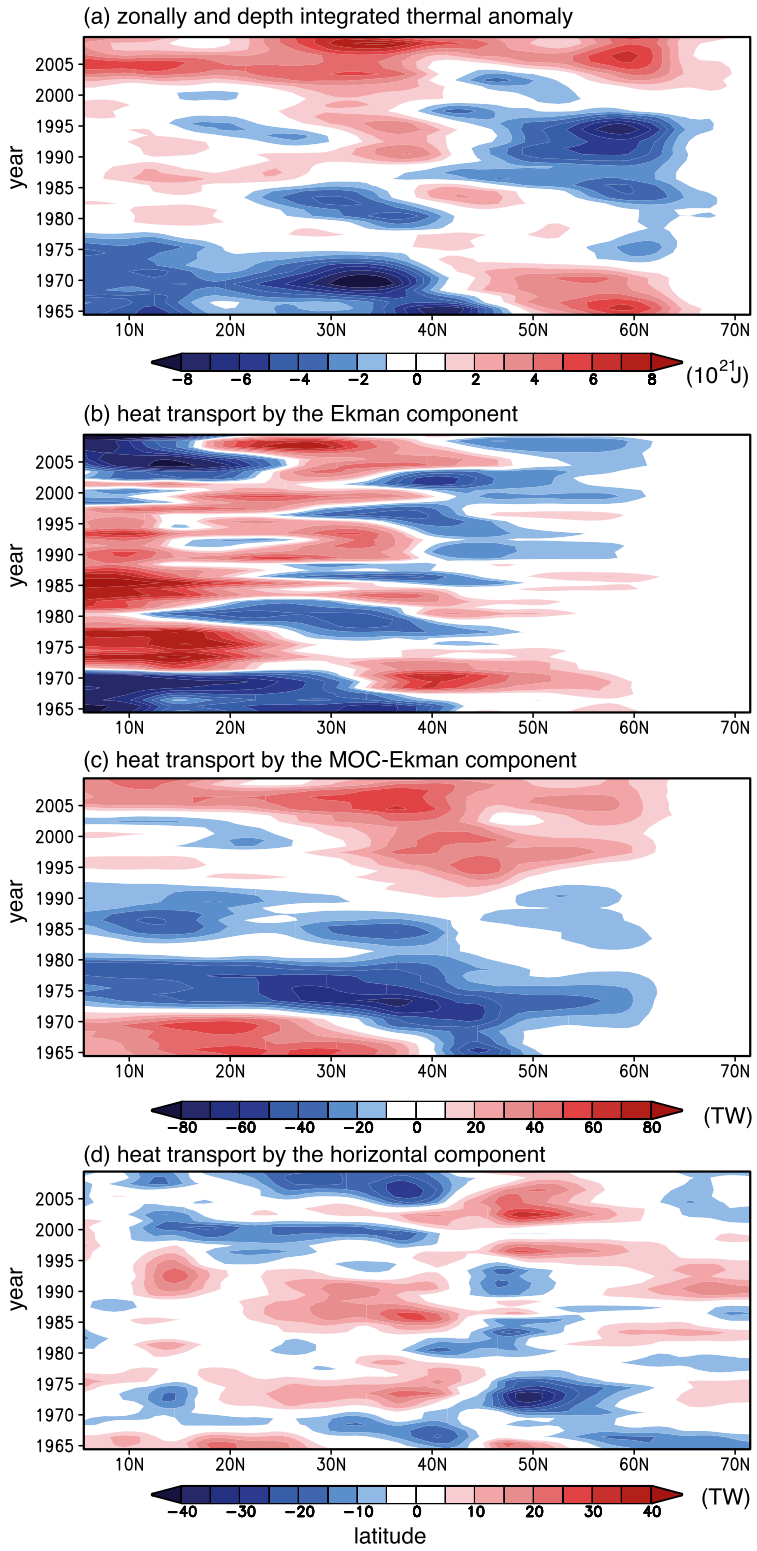

FIG. 6. Hovmöller plot of North Atlantic Ocean anomalies for (a) depth- and zonally integrated heat content Q' (y, t) (10^{21} J) and heat transport components (TW), (b) Ekman, (c) MOC-Ekman, and (d) horizontal (5°–70°N) vs time (1965–2008; plotted with a smoothing of 3-yr running mean); note the smaller scale in (d).

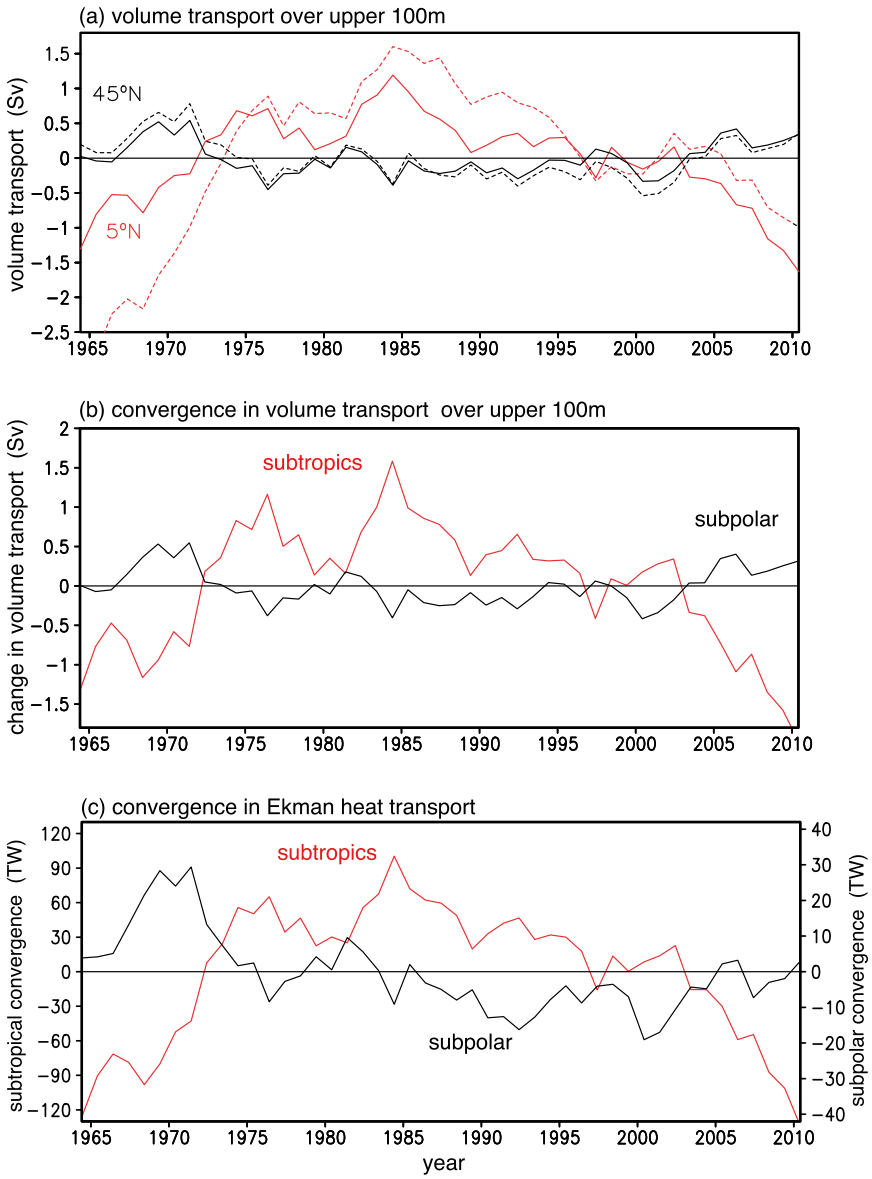

FIG. 7. Time series related to anomalies in Ekman volume and heat transfer: (a) meridional volume transport (Sv; full line) over the upper 100 m, which is dominated by the zonal integral of the Ekman transfer $-\tau_x/(\rho f)$ (dashed line); (b) convergence in meridional volume transport (Sv) over the upper 100 m and (c) Ekman heat transport convergence (TW). The transports are evaluated at 5° (red line) and 45°N (black line), the subtropical convergence is between 5° and 45°N (red line), and the subpolar convergence between 45° and 75°N (black line). Note the different scales used to emphasize the contrast between the gyres in (c).

The convergence in the volume transport over each gyre (Fig. 7b) is dominated by the transport on its equatorial side, so that the subtropical convergence broadly resembles the volume transport at 5° and the subpolar convergence resembles that at 45°N. The convergence in Ekman heat transport (Fig. 7c) varies in a broadly similar manner to the convergence in volume transport over the upper 100 m. This Ekman heat convergence has opposing signs between the subtropical and subpolar gyres, providing a subtropical loss of heat in 1960 and a gain of heat in 1985, contrasting with a weaker subpolar gain in heat in 1970 and a loss in heat in 1990.

This gyre connection between convergences of volume and heat transport carries over into the thermocline. For example, over a depth range from 100 to 1300 m, the volume transport anomalies at 5° and 45°N

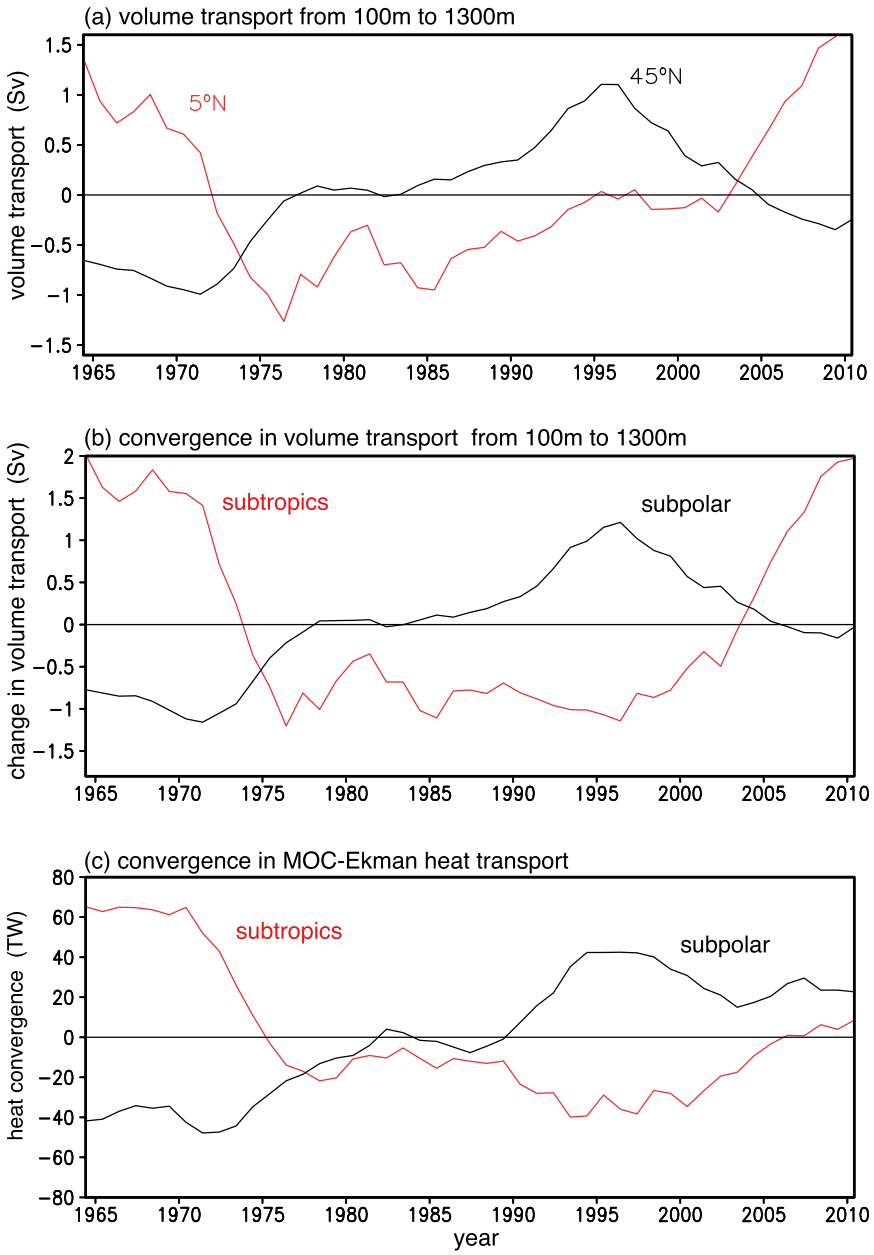

FIG. 8. Time series related to anomalies in MOC-Ekman volume and heat transfer: (a) meridional volume transport (Sv) from 100 to 1300 m; (b) convergence in meridional volume transport (Sv) from 100 to 1300 m; and (c) convergence in MOC-Ekman heat transport (TW). The transports are evaluated at 5° (red line) and 45°N (black line), the subtropical convergence is between 5° and 45°N (red line), and the subpolar convergence between 45° and 75°N (black line).

are similar in magnitude and often of opposing sign (Fig. 8a), leading to the convergences in volume transport having opposing signs in the subtropics and subpolar gyres (Fig. 8b): in the subtropics, a positive anomaly in 1960 changing to a negative anomaly in 1995, and in the subpolar region, a negative anomaly in 1970 changing to a positive anomaly in 1995. The resulting convergence in MOC-Ekman heat transport (Fig. 8c) closely follows the convergence in volume transport from 100 to 1300 m, providing a subtropical gain in heat in 1965 and a loss of heat in 1995, contrasting with a subpolar loss of heat in 1965 and a gain in heat in 1995.

In summary, variations in volume convergence are driving the changes in heat convergence, which often

have opposite signs in each gyre. Subtropical anomalies in Ekman heat convergence are typically a factor of 3 larger than the subpolar anomalies, while the anomalies in MOC-Ekman heat convergence are broadly comparable over the subtropical and subpolar gyres.

d. Thermal anomalies in the subtropical and subpolar gyres

The evolution of the depth- and zonally integrated thermal anomalies $Q'(y,t)$, over the subtropical and subpolar gyres (Fig. 9, black line) are now reconsidered in terms of the time integral of the air–sea fluxes and the different heat transport components. A long-term heat balance is assumed to occur between the climate mean air–sea flux and the divergence of the climate mean heat transport,

$$\overline{\mathcal{H}}^{t} = \rho_0 C_p \int_{-D}^{0} \frac{\partial}{\partial y} \overline{v\theta}^{x,t}\, dz \equiv \nabla \cdot \overline{(VQ)}^{t}, \qquad (6)$$

where the overbar with t represents a time average. The thermal anomalies are controlled by departures from (6), such that long-term thermal anomalies $Q'(y,t)$ from 1965 onward are given by the time integral of the convergence of the heat transport anomalies and air–sea flux anomalies, defined by

$$Q'(y,t) = Q'(y,1965) - \int_{1965}^{t} \nabla \cdot (VQ)'\, dt + \int_{1965}^{t} \mathcal{H}'\, dt, \qquad (7)$$

where the prime now denotes a departure from a time and zonal mean.

In the subtropics, there is a cool anomaly from 1965 to 1975, then changing to a warm anomaly that strengthens after 2000 (Fig. 9a, black line). The formation of the warm anomaly is not explained by the time integral of air–sea heat flux anomalies [$\mathcal{H}'$ term in (7)] from NCEP, but is closer to that suggested from ECMWF (Fig. 9a, blue and green lines).

In the subpolar gyre, there is a warm anomaly up to 1973, changing to a cold anomaly and then returning to a warm anomaly after 2000 (Fig. 9c, black line). This warming trend is not explained by the time integral of the air–sea heat fluxes anomalies from either NCEP or ECMWF (Fig. 9c, blue and green lines).

Instead, the formation of the thermal anomalies is more generally explained by the time integral of the convergence of heat transport anomalies [$-\nabla \cdot (VQ)'$ term in (7); Figs. 9b,d, red line]. The time-integrated heat convergence is achieved primarily by the Ekman transfer in the subtropical gyre (Fig. 9b, green line), augmented by the air–sea heat fluxes from ECMWF, and the MOC-Ekman transfer in the subpolar gyre (Fig. 9d, blue line). Thus, the contrasting thermal anomalies in the subtropical and subpolar gyres are primarily induced by convergences of different heat transport components.

e. Correlations between the local heat content tendency and the heat convergences

To gain insight into the spatial pattern of how the thermal anomalies respond to heat transport, the detrended local heat content tendency is correlated with the detrended area-integrated heat convergence for each gyre; in interpreting these correlation maps, some caution is required over the extension of the Gulf Stream, where the reliability of the model assimilation is lacking due to the coarse resolution.

Over the central subtropical gyre (5°–45°N), there is a high correlation between the local heat content tendency and the heat convergence anomalies (Fig. 10a), the latter primarily created by Ekman heat convergence (Fig. 10b) augmented by the MOC-Ekman heat transport on the northern flank of the subtropical gyre (Fig. 10c). The contribution of the horizontal heat convergence is relatively unimportant over the subtropical gyre.

Over the subpolar gyre (45°–75°N), there is a high correlation between the detrended local heat content tendency along the northern rim of the subpolar gyre and the heat convergence over the entire subpolar gyre (Fig. 10a). This correlation pattern reflects the contribution of the horizontal heat supply along the northern rim of the subpolar gyre (Fig. 10d) augmented by the Ekman transfer over the intergyre boundary and the MOC-Ekman heat convergence over the eastern side of the subpolar gyre (Fig. 10c).

In summary, the local heat content tendency has different correlation patterns with the separate components of the heat transport convergence, consistent with the view that each component has a particular spatial imprint, with the wind-driven Ekman convergence particularly affecting the central part of the subtropical gyre and the MOC-Ekman and horizontal convergences affecting the eastern and northern sides of the subpolar gyre.

f. Correlations with atmospheric winds and atmospheric modes

The variability of the ocean heat content anomaly and its tendency, and the convergence in heat transport anomalies, are now connected to the large-scale wind forcing. For the subtropics, there is a negative correlation between the detrended anomalies in gyre-integrated heat

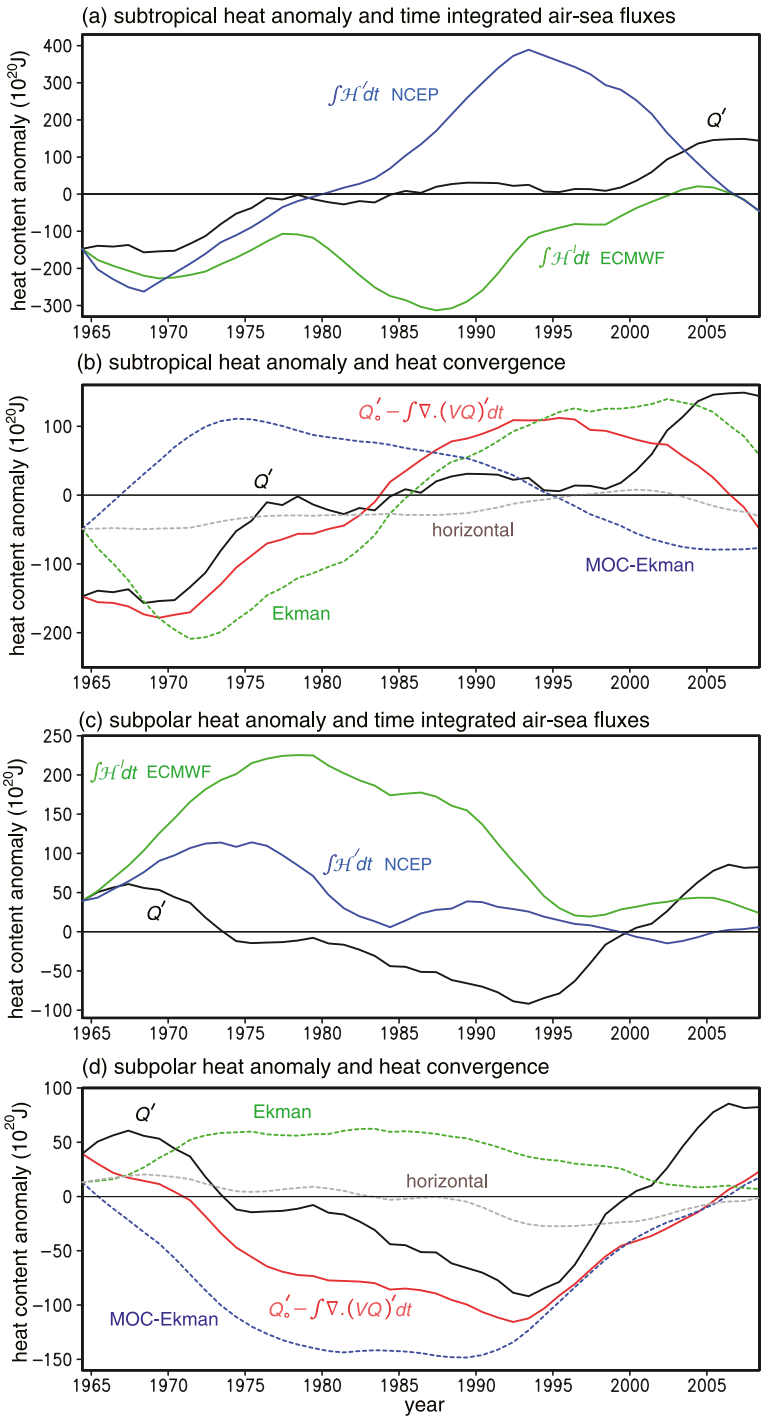

FIG. 9. Time series for depth- and zonally integrated heat content anomaly $Q'(t)$ (10^{20} J; black line) first for the tropics and subtropics (5°–45°N) and second the subpolar region (45°–75°N) from 1965 to 2010 vs (a),(c) the time integral of the temporal anomalies in air–sea fluxes from NCEP (blue) and ECMWF (green) and (b),(d) the time integral of the temporal anomalies in heat convergence $Q'(1965) - \int_{1965}^{t} \nabla \cdot (VQ)' \, dt$ (red line) together with the contribution to the thermal anomaly from the Ekman (green dashed), MOC-Ekman (blue dashed), and horizontal (gray dashed) components based on annual anomalies (evaluated with a 5-yr running mean).

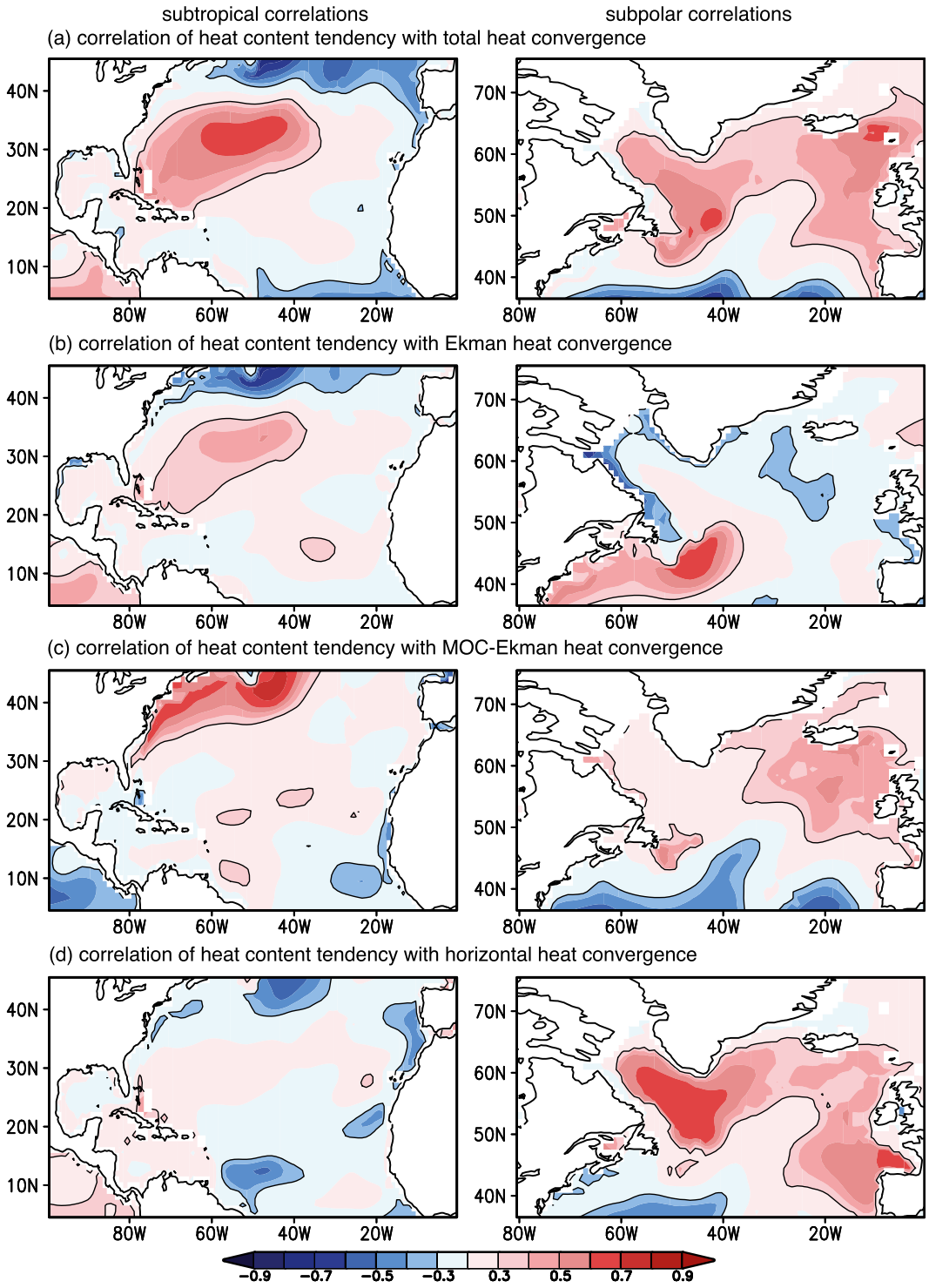

FIG. 10. Correlation plots between the time series for the local tendency in depth-integrated heat content and the anomalies in heat supply over (left) the tropics and subtropics (5°–45°N) and (right) the subpolar region (45°–75°N) based on annual anomalies from 1965 to 2010 (with a 5-yr running mean and detrended): for (a) total heat convergence $-\int_{1965}^{t} \nabla \cdot (VQ)' \, dt$, (b) Ekman heat convergence, (c) MOC-Ekman heat convergence, and (d) horizontal heat convergence. Full lines show correlations for ±0.3 (>95% confidence limit).

TABLE 3. Correlations of Q', $\partial Q'/\partial t$, and $-\nabla \cdot (VQ)'$ and its components, with time series for area-integrated wind stress curl $\nabla \times \tau$, zonally integrated eastward wind stress $\int \tau_x \, dx$, and atmospheric modes (NAO and EA). Heat content anomalies are averaged over the tropics and subtropics (5°–45°N) and subpolar region (45°–75°N), and the wind stress curl and heat transport convergences are evaluated for the same latitude ranges. Zonally integrated wind stress is averaged over gyre boundaries at 10°–20°N when correlated with the subtropics and at 45°–55°N for the subpolar region. All fields are detrended, 5-yr running means are applied, and the correlations are evaluated for the period 1965–2010. Correlations are shown in italic if greater than ±0.24 (90% confidence limit), roman if greater than ±0.34 (98% confidence limit), and in boldface if greater than ±0.37 (99% confidence limit).

Heat anomaly, heat transport convergence	Subtropical				Subpolar			
	$\nabla \times \tau$	$\int \tau_x \, dx$	NAO	EA	$\nabla \times \tau$	$\int \tau_x \, dx$	NAO	EA
Q'	−0.37	**−0.43**	—	*0.30*	**−0.54**	**−0.78**	**−0.79**	**−0.57**
$\partial Q'/\partial t$	—	**−0.39**	—	—	—	−0.35	**−0.47**	—
$-\nabla \cdot (VQ)'$ for:								
Total	**−0.60**	**−0.79**	**0.73**	*0.34*	**−0.55**	**−0.69**	**−0.57**	*−0.34*
MOC	**−0.52**	**−0.76**	**0.63**	*0.29*	**−0.38**	−0.36	—	*−0.26*
Ekman	**−0.66**	**−0.74**	**0.71**	**0.49**	**−0.84**	**−0.80**	**−0.54**	**−0.52**
MOC-Ekman	**0.67**	**0.50**	**−0.62**	**−0.64**	—	*0.25*	—	—
Horizontal	**−0.54**	**−0.44**	**0.68**	*0.33*	**−0.41**	**−0.69**	**−0.86**	—

content and wind forcing (Table 3), −0.37 for the area-integrated wind stress curl and −0.43 for the zonally integrated wind stress on the equatorial flank of the gyre (10°–20°N). Likewise, there is a negative correlation between the tendency of the thermal anomaly and the wind stress on the equatorial flank of −0.39. This relationship is consistent with the large negative correlations between the subtropical heat convergence and wind forcing, −0.60 for wind stress curl and −0.79 for the wind stress on the equatorial flank. This latter connection is mainly due to the automatic link between the wind stress and the convergences in the MOC and Ekman heat transport with correlations of −0.76 and −0.74, augmented by a negative correlation with the convergence in horizontal heat transport of −0.44. Hence, a strengthening in the easterly trade winds (more negative) is associated with an enhanced Ekman convergence of heat over the subtropics, acting to increase the subtropical heat storage.

For the subpolar gyre, there are also negative correlations between the gyre-integrated heat content and wind forcing, −0.54 for wind stress curl and −0.78 for the zonally integrated wind stress on the subtropical/subpolar boundary (45°–55°N). Likewise, there is a weaker negative correlation between the tendency of the thermal anomaly and wind stress on the intergyre boundary of −0.35. This relationship is also consistent with the negative correlations between the subpolar heat convergence and wind forcing, −0.55 for wind stress curl and −0.69 for the zonally integrated wind stress on the intergyre boundary. Again, there is an automatic negative correlation between the wind stress and the convergence in Ekman heat transport of −0.80, which is enhanced by a negative correlation with the horizontal heat convergence of −0.69. Thus, an increase in the westerlies is associated with both reduced Ekman and horizontal heat convergences over the subpolar gyre, acting to reduce the subpolar heat storage.

The correlation with the atmosphere can also be viewed in terms of the two leading empirically orthogonal modes of variability over the basin, the North Atlantic Oscillation (NAO) (Hurrell 1995) and the east Atlantic (EA) pattern (Barnston and Livezey 1987); for winter, a positive NAO represents a larger pressure contrast between Iceland/Greenland and the Azores, and a positive EA represents a lower pressure over the central part of the North Atlantic (50°N, 40°W) and a higher pressure in the tropical North Atlantic. For the subtropics, a more positive NAO is associated with increased Ekman, horizontal, and MOC heat convergences (with correlations of 0.71, 0.68, and 0.63, respectively) and a similar signed, weaker response with the EA (with correlations of 0.49, 0.33, and 0.29; Table 3). For the subpolar gyre, a more positive NAO is correlated with a decrease in the horizontal and Ekman heat convergences (with values of −0.86 and −0.54), as well as a more positive EA with a decrease in the Ekman heat convergence (with a value of −0.52); the MOC or MOC-Ekman does not significantly correlate with the NAO, and MOC only correlates weakly and negatively with the EA.

These correlations can be understood by a more positive NAO or EA being associated with a strengthening in the easterly trade winds on the equatorial flank of the subtropical gyre and an increase in the northward Ekman heat transport, which then provides a greater heat convergence in the subtropical gyre. Conversely, a strengthening in the westerly winds on the subtropical/subpolar boundary leads to an increase in the southward Ekman transport and a decrease in the heat convergence in the subpolar gyre. This Ekman response is often reinforced by the changes in the horizontal heat convergence.

In summary, the subtropical and subpolar thermal anomalies both negatively correlate with the wind stress on their equatorial boundary: subtropical heat content increases with more easterly trade winds and subpolar heat content decreases with stronger westerlies.

6. Discussion

The North Atlantic experiences significant basinwide changes in surface temperatures, which are generally viewed as being controlled by the meridional overturning circulation. Our diagnostics of ocean heat content over the last 60 years emphasize though how thermal anomalies often have an opposing sign in the subtropical and subpolar gyres. These thermal anomalies are not restricted to the sea surface and extend to depths of 1–2 km into the thermocline, implying an advective origin. To understand how these thermal anomalies evolve on decadal time scales, historical annual temperature and salinity data from 1965 to 2010 are dynamically assimilated into a 1°-resolution MIT general circulation model. While this approach ignores seasonality and finer-scale circulations, our model diagnostics suggest that these thermal anomalies are controlled primarily by changes in ocean heat convergence, augmented by the poorly known air–sea fluxes.

At first sight, the gyre-scale contrast in the thermal anomalies appears at odds with the canonical view of the meridional overturning circulation providing a basinwide response. To unravel this conundrum, we separate the meridional heat transport into different components in a mass-conserving framework: a wind-driven Ekman heat transport, an MOC-Ekman heat transport, and a horizontal heat transport. Each component provides a dominant contribution over a different region to the meridional heat transport: for a climate mean, the Ekman response dominates at low latitudes, the MOC-Ekman response at midlatitudes, and the horizontal transport at high latitudes. Wind-driven changes in the Ekman and horizontal heat transport are clearly expected to have a different response in the subtropical and subpolar gyres. Likewise, temporal changes in the MOC often have a contrasting gyre response associated with the large-scale wind forcing, as previously diagnosed from density data for 1950–70 and 1980–2000 (Lozier et al. 2010) and revealed in model circulation experiments on interannual and decadal time scales (Bingham et al. 2007; Biastoch et al. 2008).

For the subtropics, the sign of the thermal anomalies varies over several decades from cool in 1970 to warm in 2000. The cool anomaly corresponds to a reduction in Ekman heat convergence and the warm anomaly to an increase in Ekman heat convergence. Thus, changes in atmospheric winds are central in altering the subtropical heat convergence and in controlling the sign of the decadal thermal anomalies; as previously argued for, subtropical heat content varies between two different periods of the NAO (Lozier et al. 2008). However, over the last 10 years, the subtropical warming is greater than that provided by the ocean heat convergence and needs to be augmented by an increase in heat input from the atmosphere, as suggested by ERA-Interim.

In the subpolar gyre, the sign of the thermal anomalies also varies, but with an opposing sign to the subtropics prior to 2000: warm in 1970, cool in 1990, and again warm in 2005. The change in sign of the thermal anomaly in the subpolar gyre reflects a change in the heat convergence, mainly due to the MOC-Ekman component, varying from a negative anomaly in 1975 to a positive anomaly in 1995. Taking that view further, Robson et al. (2012), employing a coupled atmosphere–ocean model, argue that a surge in the northward heat transport led to the rapid warming of the subpolar North Atlantic in the mid-1990s.

The gyre-scale contrasts in the sign of these thermal anomalies are probably a dynamical response to changes in the surface winds. Mechanistically, a general strengthening of the winds is expected to increase Ekman heat convergence and heat content for the subtropical gyre. At the same time, the increase in Ekman downwelling is likely to deepen the thermocline westward and lighten the density along the western boundary of the subtropical gyre. The resulting thermal-wind shear between the western and eastern sides of the basin then reduces the northward MOC-Ekman volume transport in the subtropical gyre. Conversely, for the subpolar gyre, an increase in the winds is expected to increase upwelling, reduce heat content, and increase density along the western boundary. The resulting thermal-wind shear then increases the northward MOC-Ekman volume transport in the subpolar gyre. Hence, variations in the strength of the winds naturally lead to opposing signs in the thermal anomalies, Ekman heat convergence, and MOC-Ekman volume transport in each gyre.

In conclusion, the imprint of changes in the surface winds leads to gyre-scale thermal anomalies with contrasting signs in the subtropical and subpolar gyres, which can often obscure any basinwide warming response. This wind-driven control of the thermal anomalies is probably ultimately achieved by the position and strength of the jet stream and persistent atmospheric blocks (Woollings et al. 2010; Häkkinen et al. 2011).

Acknowledgments. RGW and VR were supported by UK Natural Environment Research Council (NER/T/S/

2002/00439), DS by the joint DECC/DEFRA Met Office Hadley Centre Programme (GA001101), and MSL by the U.S. National Science Foundation. We are grateful to two referees for critical comments that strengthened the study, and to Justin Buck for advice on the Argo data. We also acknowledge use of ECMWF and NCEP reanalysis data, and comparison with ECCO inverse model analyses.

APPENDIX

Reconstructing the Historical Data and Heat Balance

a. Gridded analyses of historical temperature and salinity data

The global ocean temperature and salinity analyses were provided by the Met Office Hadley Centre. They were created by statistical interpolation of the available hydrographic observations and recent Argo data from the Met Office EN3 dataset (Ingleby and Huddleston 2007) using covariances to interpolate between observational data (Smith and Murphy 2007). This approach provides monthly mean fields since 1950, at a resolution of 1.25° and 20 vertical levels, 7 of which are in the upper 100 m. Smith and Murphy (2007) demonstrated in idealized tests that even with very sparse observations typical of the 1950s, it is potentially possible to create accurate analyses, with correlations of greater than 0.7 between analyzed and true monthly fields. However, this method relies on accurate covariances. The analyses used here are an update to the original version (Smith and Murphy 2007) in that improved covariances were obtained using an iterative approach, as follows.

For the first iteration, covariances were computed from a nine member ensemble of the Hadley Centre Coupled Model, version 3 (HadCM3) simulations of the period 1950–99. Each ensemble member used a different variant of HadCM3, created by perturbing poorly constrained parameters of the atmospheric physics schemes (Collins et al. 2010). The accuracy of model covariances cannot be assessed for subsurface data because the observations are too sparse. However, sea surface temperature (SST) model covariances were evaluated and found to be in good agreement with a compilation of historical surface temperature data, the Hadley Centre Sea Ice and Sea Surface Temperature dataset (HadISST). Furthermore, SST covariances from the nine-member ensemble agreed better with HadISST than those computed from the model version with standard parameter settings.

For the second iteration, covariances were computed directly from the analyses of the period 1950–2006 obtained in the first iteration. These covariances are potentially more accurate than the model covariances used in the first iteration because they have been influenced by the real observations. This approach was tested by performing data withholding experiments for the data-rich period 2007–10, in which analyses created using all available observations were taken as the truth and compared with analyses created using subsampled observations at locations typical of the 1960s. The subsampled analyses based on the covariances used in the second iteration were found to be more accurate than those based on the first iteration. One additional iteration, using covariances computed from the second iteration analyses, was performed to create the final analyses used in this study.

For most of the historical period, subsurface observations were dominated by expendable bathythermographs (XBTs). Biases in these XBT data have recently been identified (Domingues et al. 2008; Levitus et al. 2009; Ishii and Kimoto 2009) and were corrected in the analyses used here. Since 2001 there has been an increasing contribution from Argo floats (Roemmich and Owens 2000), increasing from 2500 to 16 000 profiles a year from 2001 to 2010 in the North Atlantic. It is possible that unknown biases or other problems with the Argo data might be present. We therefore repeated the analyses for the period 2000–09, but exclude Argo data. The analyses with and without Argo data are remarkably similar (Figs. 1a and A1a). In both cases, the upper thermocline warms over this decade, although the analysis including Argo data is slightly warmer at depths of 1500 m (Fig. A1b).

While there are ongoing calibrations and corrections for any new measurement technique (Barker et al. 2011), the broad agreement between the analyses with and without Argo data suggests that any errors associated with the Argo data are smaller than the thermal anomalies emerging on a decadal time scale.

b. Dynamical assimilation method

To obtain estimates of how the thermal anomalies are controlled and ocean heat transport is partitioned; we adopt the following procedure to assimilate the historical temperature and salinity data in a simple manner:

1) The MIT general circulation model (Marshall et al. 1997) is initialized with the Hadley Centre analyses of temperature and salinity data (Smith and Murphy 2007). MITgcm is on a 1° grid with 23 vertical levels over the globe, while the Hadley Centre analyses are on a slightly coarser 1.25° grid with 20 vertical levels, so that model data are linearly interpolated from the original analyses.

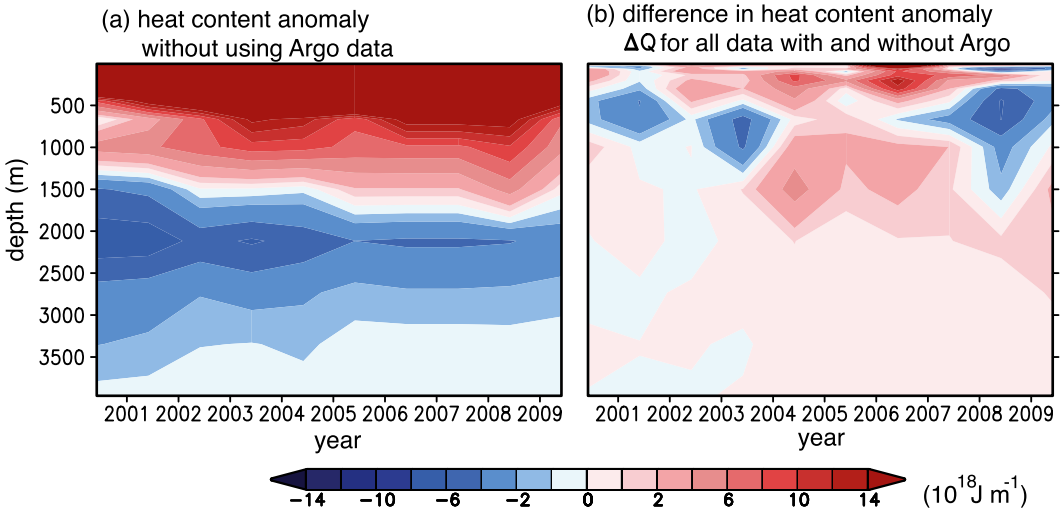

FIG. A1. Evolution of North Atlantic zonally integrated heat content anomaly (10^{18} J m^{-1}) vs depth (m) from 2000 to 2009 (as in Fig. 1a): (a) omitting any Argo data and (b) the difference in the heat content anomaly between the assimilations including and excluding the Argo data.

2) The model is integrated forward in time with monthly forcing taken from monthly mean wind stresses from NCEP for each year. The model includes a weak artificial relaxation of temperature and salinity to the initial annually averaged temperature and salinity data on a 3-yr time scale, which acts to minimize model drift.
3) Our estimates of the heat transport and changes in heat transport are based on dynamically adjusted model fields for velocity and temperature after an initial spinup of 1 month and then a further 12 months to cover a full annual cycle.

Our algorithm is tested by comparing our estimates of changes in the MOC between two periods, 2003–07 minus 1993–97. Our methodology is applied to estimate the MOC changes (Fig. A2a, lines) from synthetic density data taken from a global inverse model, the Estimating the Circulation and Climate of the Ocean Global Ocean Data Assimilation Experiment (ECCO-GODAE), and then compared with that diagnosed directly from the velocities (Fig. A2a, crosses) from ECCO-GODAE. The mismatch in the MOC anomalies and the truth is generally less than ±0.4 Sv, apart from around 40°N where the error reaches ±0.6 Sv. The error slightly increases with the length of the model integration, increasing with the choices from 1–12 to 7–18 months. At the same time, the choice of model integration alters the heat transport. The total heat transport is less when the model integration is restricted to 12 months, but converges to a slightly higher estimate if there is an initial spinup of 1 month or longer and then followed by 12 months to evaluate the annual cycle (Fig. A2b); the lower initial estimate of the heat transport is associated with a lower heat transport by the vertical cell. As a compromise choice, we then choose to diagnose the heat transport using an initial spinup of 1 month followed by an integration of 12 months.

In comparison, a longer initial adjustment time scale of 6 months, rather than 1 month, is chosen previously in Lozier et al. (2010) because of their initializing the MIT general circulation model with noisier hydrographic data.

c. *Sensitivity in reconstructing the heat balance to temperature perturbations*

To obtain estimates of the sensitivity in the reconstruction of the heat balance (Figs. 2 and 3), 36 ensemble calculations are performed using the global MIT circulation model initialized with perturbations in the historical temperature data from the Met Office. The standard errors for the annual temperature in 1985 typically reach 0.4°C at 5 m, decreasing to 0.25°C at 500 m, 0.15°C at 1000 m, and 0.05°C at 2000 m. The corresponding standard errors for salinity typically reach 0.2 g kg^{-1} at 5 m, decreasing to 0.03 g kg^{-1} at 500 m, 0.02 g kg^{-1} at 1000 m, and 0.005 g kg^{-1} at 2000 m. The circulation is sensitive to perturbations in density, but some of the temperature and salinity changes are likely to be partially compensating. Consequently, we choose to only include perturbations in temperature, as that directly affects heat content and probably provides an upper bound for the density changes. The reconstructions are performed for two periods centered either on 1985 or 1998. For each

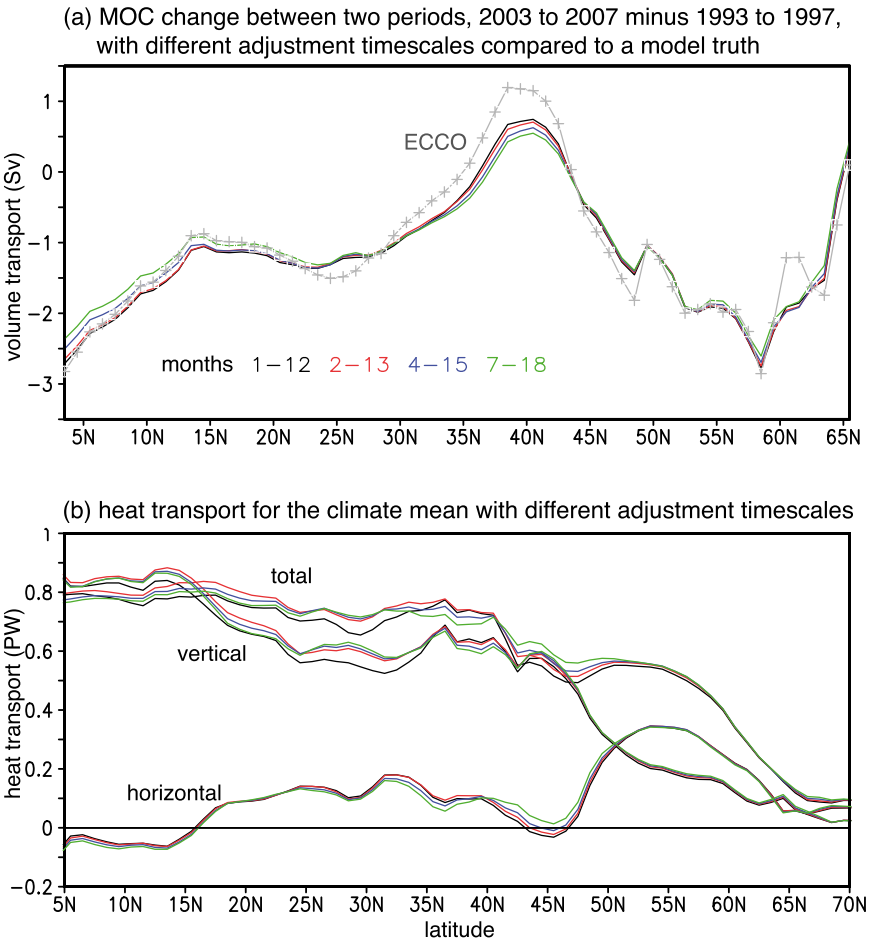

FIG. A2. Tests of the model adjustment. (a) MOC change between two 5-yr periods, 2003–07 minus 1993–97, for a model truth (ECCO; crosses) and for different choices for the time span of model adjustment, 1–12 (black), 2–13 (red), 4–15 (blue), and 7–18 (green) months. (b) Heat transport for the climate mean (PW) for the total, vertical, and horizontal for these different choices for the time span of model adjustment.

ensemble, the temperature data are perturbed over 5° squares based on its standard error from the original Met Office analysis (with the salinity data unaltered) multiplied by randomly generated numbers between 0.5 and 1 or between −0.5 and −1. The resulting heat content tendency $\partial Q'/\partial t$ is evaluated over a 5-yr period by the difference between the two adjoining 5-yr periods. The convergence of the heat transport anomalies $-\nabla \cdot (VQ)'$ is then evaluated from an average of these two 5-yr periods.

This procedure for estimating the heat content tendency and convergence in heat transport anomaly are then applied for the two periods centered on 1985 and 1998 (Table 2). Including perturbations in the historical temperature data leads to the heat content tendency altering by up to ±7 TW for the subtropics and by ±3 TW in the subpolar gyre. There are larger changes in the convergence in the heat transport over the gyres, reaching ±12 TW for the subtropics and ±8 TW over the subpolar gyre.

These estimates are only included as a guide to the temperature sensitivity based on the historical data. The actual error in our analyses will be even larger, increased by variations in the winds together with systematic errors and offsets in the reconstruction of the circulation using the model assimilation method.

REFERENCES

Anderson, D. L. T., and A. E. Gill, 1975: Spin-up of a stratified ocean, with application to upwelling. *Deep-Sea Res.,* **22,** 583–596.

Barker, P. M., J. R. Dunn, C. M. Domingues, and S. E. Wijffels, 2011: Pressure sensor drifts in Argo and their impacts. *J. Atmos. Oceanic Technol.,* **28,** 1036–1049.

Barnston, A. G., and R. E. Livezey, 1987: Classification, seasonality, and persistence of low-frequency atmospheric circulation patterns. *Mon. Wea. Rev.,* **115,** 1083–1126.

Biastoch, A., C. W. Böning, J. Getzlaff, J.-M. Molines, and G. Madec, 2008: Causes of interannual–decadal variability in the meridional overturning circulation of the midlatitude North Atlantic Ocean. *J. Climate,* **21,** 6599–6615.

Bingham, R. J., C. W. Hughes, V. Roussenov, and R. G. Williams, 2007: Meridional coherence of the North Atlantic meridional overturning circulation. *Geophys. Res. Lett.,* **34,** L23606, doi:10.1029/2007GL031731.

Boyer, T. P., and Coauthors, 2006: *World Ocean Database 2005.* NODC Atlas NESDIS 60, S. Levitus, Ed., U.S. Government Printing Office, 190 pp.

Bryden, H., and S. Imawaki, 2001: Ocean heat transport. *Ocean Circulation and Climate,* G. Siedler, J. Church, and J. Gould, Eds., International Geophysics Series, Vol. 77, Academic Press, 455–474.

Collins, M., B. B. B. Booth, B. Bhaskaran, G. R. Harris, J. M. Murphy, D. M. H. Sexton, and M. J. Webb, 2010: Climate model errors, feedbacks and forcings: A comparison of perturbed physics and multi-model ensembles. *Climate Dyn.,* **36,** 1737–1766, doi:10.1007/s00382-010-0808-0.

Cunningham, S. A., and Coauthors, 2007: Temporal variability of the Atlantic meridional overturning circulation at 26.5°N. *Science,* **317,** 935–938.

Czaja, A., and J. Marshall, 2006: The partitioning of poleward heat transport between the atmosphere and ocean. *J. Atmos. Sci.,* **63,** 1498–1511.

Domingues, C., J. A. Church, N. White, P. Gleckler, S. Wijffels, P. Barker, and J. Dunn, 2008: Improved estimates of upper-ocean warming and multi-decadal sea-level rise. *Nature,* **453,** 1090–1093, doi:10.1038/nature07080.

Gill, A. E., and P. P. Niller, 1973: The theory of the seasonal variability in the ocean. *Deep-Sea Res.,* **20,** 141–177.

Greatbatch, R. J., A. F. Fanning, and A. D. Goulding, 1991: A diagnosis of interpentadal circulation changes in the North Atlantic. *J. Geophys. Res.,* **96,** 22 009–22 023.

Häkkinen, S., P. Rhines, and D. Worthen, 2011: Atmospheric blocking and Atlantic multidecadal ocean variability. *Science,* **334,** 655–659.

Hall, M., and H. Bryden, 1982: Direct estimates and mechanisms of ocean heat transport. *Deep-Sea Res.,* **29,** 339–359.

Hurrell, J., 1995: Decadal trends in the North Atlantic Oscillation: Regional temperatures and precipitation. *Science,* **269,** 676–679.

Ingleby, B., and M. Huddleston, 2007: Quality control of ocean temperature and salinity profiles: Historical and real-time data. *J. Mar. Syst.,* **65,** 158–175.

Ishii, M., and M. Kimoto, 2009: Reevaluation of historical ocean heat content variations with time-varying XBT and MBT depth bias corrections. *J. Oceanogr.,* **65,** 287–299.

Jayne, S. R., and J. Marotzke, 2001: The dynamics of ocean heat transport variability. *Rev. Geophys.,* **39,** 385–411.

Kanzow, T., and Coauthors, 2007: Observed flow compensation associated with the MOC at 26.5°N in the North Atlantic. *Science,* **317,** 938–941.

Klinger, B. A., and J. Marotzke, 2000: Meridional heat transport by the subtropical cell. *J. Phys. Oceanogr.,* **30,** 696–705.

Levitus, S., J. I. Antonov, T. P. Boyer, R. A. Locarnini, H. E. Garcia, and A. V. Mishonov, 2009: Global ocean heat content 1955–2008 in light of recently revealed instrumentation problems. *Geophys. Res. Lett.,* **36,** L07608, doi:10.1029/2008GL037155.

——, and Coauthors, 2012: World ocean heat content and thermosteric sea level change (0–2000 m), 1955–2010. *Geophys. Res. Lett.,* **39,** L10603, doi:10.1029/2012GL051106.

Lozier, M. S., S. Leadbetter, R. G. Williams, V. Roussenov, M. S. C. Reed, and N. J. Moore, 2008: The spatial pattern and mechanisms of heat-content change in the North Atlantic. *Science,* **319,** 800–803.

——, V. Roussenov, M. S. C. Reed, and R. G. Williams, 2010: Opposing decadal changes for the North Atlantic meridional overturning circulation. *Nat. Geosci.,* **3,** 728–734.

Marotzke, J. R., K. Giering, Q. Zhang, D. Stammer, C. Hill, and T. Lee, 1999: Construction of the adjoint MIT ocean general circulation model and application to Atlantic heat transport sensitivity. *J. Geophys. Res.,* **104,** 29 529–29 547.

Marshall, J., C. Hill, L. Perelman, and A. Adcroft, 1997: Hydrostatic, quasi-hydrostatic, and nonhydrostatic ocean modeling. *J. Geophys. Res.,* **102,** 5733–5752.

Mellor, G. L., C. R. Mechoso, and E. Keto, 1982: A diagnostic calculation of the general circulation of the Atlantic Ocean. *Deep-Sea Res.,* **29A,** 1171–1192.

Piecuch, C. G., and R. M. Ponte, 2012: Importance of circulation changes to Atlantic heat storage rates on seasonal to interannual time scales. *J. Climate,* **25,** 350–362.

Renfrew, I. A., G. W. K. Moore, P. S. Guest, and K. Bumke, 2010: A comparison of surface layer and surface turbulent flux observations over the Labrador Sea with ECMWF analyses and NCEP reanalyses. *J. Phys. Oceanogr.,* **32,** 383–400.

Rhein, M., and Coauthors, 2011: Deep-water formation, the subpolar gyre, and the meridional overturning circulation in the subpolar North Atlantic. *Deep-Sea Res. II,* **58,** 1819–1832.

Robson, J., R. Sutton, K. Lohmann, D. Smith, and M. D. Palmer, 2012: Causes of the rapid warming of the North Atlantic Ocean in the mid-1990s. *J. Climate,* **25,** 4116–4134.

Roemmich, D., and W. B. Owens, 2000: The Argo project: Global ocean observations for understanding and prediction of climate variability. *Oceanography,* **13,** 45–50.

Smith, D. M., and J. M. Murphy, 2007: An objective ocean temperature and salinity analysis using covariances from a global climate model. *J. Geophys. Res.,* **112,** C02022, doi:10.1029/2005JC003172.

——, R. Eade, N. J. Dunstone, D. Fereday, J. M. Murphy, H. Pohlmann, and A. A. Scaife, 2010: Skilful multi-year predictions of Atlantic hurricane frequency. *Nat. Geosci.,* **3,** 846–849, doi:10.1038/ngeo1004.

Talley, L., 1999: Some aspects of ocean heat transport by the shallow, intermediate and deep overturning circulations. *Mechanisms of Global Climate Change at Millennial Time Scales, Geophys. Monogr.,* Vol. 112, Amer. Geophys. Union, 1–22.

Woollings, T., A. Hannachi, and B. Hoskins, 2010: Variability of the North Atlantic eddy-driven jet stream. *Quart. J. Roy. Meteor. Soc.,* **136,** 856–868.